Understanding the Interfacial Structures–Chemistry Relationships in Solid Oxide Fuel Cells (SOFC)

(Final Report for Grant Nunber DE-FG02-06ER15837)
PI: Meilin Liu
Georgia Institute of Technology
Atlanta, GA 30332-0245

A. Brief Summary of Technical Progress

Cr-Poisoning from metallic interconnects:[1] The formation of Cr-containing contaminants such as $SrCrO_4$, $(Mn/Cr)_3O_4$, Cr_2O_3, and Ag_2CrO_4 on LSM cathode surfaces have been observed by *in situ experiments*[1]. Vapor phase chromium oxyhydroxides chemically reacted with the LSM, producing $SrCrO_4$ and $(Mn/Cr)_3O_4$. We are the first research group to produce *in situ* spectroscopic data directly observing the contaminating Cr-species as they form at high temperature, without possible error that accompanies conventional *ex situ* measurement due to reactions and phase changes during the sample cooling process.

Coking on anodes exposed to carbon-containing fuels:[2] Carbon deposition on the anode lends itself readily to *in situ* measurements. All major carbon allotropes (diamond, graphite, graphene, carbon nanotubes, carbon black, diamondlike carbon) are Raman-active. Based on the presence and relative intensity of different first order and second order peaks, these phases can be distinguished from one another using Raman spectroscopy. Walker *et al.* were the first to develop and demonstrate a Raman microscope system for studying carbon formation on nickel SOFC anodes. However, their system lacks the ability to perform Raman mapping since they cannot adroitly maneuver their sample because it is contained within a vertical clamp-style furnace. In contrast, our sample chamber is mounted on an X-Y-Z motorized stage that can move in 20 nm increments. We have studied the formation of amorphous carbon on various types of anodes: porous Ni/YSZ cermets, dense Ni/YSZ composites, micro-patterned Ni and Cu electrodes on YSZ substrates. Carbon deposition was detected under methane and propane fuel gases at various temperatures

Sulfur poisoning of anodes exposed to H_2S contaminated fuel gas [2-6]: Our previous studies have demonstrated that *in situ* Raman spectroscopy may be used to follow the phase transformation of electrode materials upon exposure to sulfur-containing gases under fuel cell operating conditions. We have performed *in situ* Raman analyses on Ni-YSZ anodes exposed to H_2S-contaminated fuels under typical SOFC operation conditions. It was found that heazlewoodite (Ni_3S_2), millerite (NiS), polydymite (Ni_3S_4), and pyrite (NiS_2) were observed on Ni surface using Raman spectra, when the temperature was brought below 400^{o}C. These nickel sulfides decomposed to Ni and elemental sulfur upon heating up to higher temperatures, although the morphology of the Ni grains may have significantly changed as a result of the preceding reactions.

Oxygen Reduction on the cathode surface:[7-9] Raman techniques have been used to investigate oxygen reduction at the cathode. Studying the oxygen reduction mechanism at the cathode necessarily involves observing surface oxygen species. We have been successful in

detecting surface peroxide, O_2^{2-}, and superoxide, O_2^-, species on CeO_2 powder. Ceria is a good test material for many reasons: (1) it is the base material for GDC, a leading low temperature electrolyte candidate material, (2) some research groups are looking into the incorporation of CeO_2 as the ionically conducting ceramic phase for a cermet-based anode, and (3) its fluorite structure (with no dopants) is easy to simulate when performing test quantum chemical calculations to verify peak assignments in measured Raman spectra.

New materials with excellent tolerance to coking and H_2S poisoning [2]: New anode materials of Ni-$BaZr_{0.1}Ce_{0.7}Y_{0.2-x}Yb_xO_{3-\delta}$ have been developed for solid oxide fuel cells (SOFCs). The mixed ion conductor, $BaZr_{0.1}Ce_{0.7}Y_{0.2-x}Yb_xO_{3-\delta}$, exhibits high ionic conductivity at relatively low temperatures (500° to 700°C), which allows rapid transport of both protons and oxide ion vacancies. The new anode shows excellent tolerance to coking and sulfur poisoning. The ability to resist deactivation by sulfur and coking appears linked to the mixed conductor's enhanced catalytic activity for sulfur oxidation and hydrocarbon cracking and reforming, as well as enhanced water adsorption capability.

Catalytic and transport properties of $La_{0.5}Sr_{0.5}BO_{2.75}$ (B=Cr, Mn, Fe, Co)[7]: Understanding the mechanisms of the interactions between oxygen species and MIEC cathode surfaces are crucial to achieving rational design of high-performance cathode materials for SOFCs. The bond strength between intermediate species and surfaces plays a significant role in understanding catalytic activity of surfaces. To examine the interactions of oxygen species with four MIEC cathode materials, we constructed the (1 0 0) surface for each, which is energetically the most stable one among the low-index (1 1 0), (1 1 0), and (1 0 0) surfaces. Then, we carried out 2D slab-model calculations based on the four-layer (1 0 0) surfaces to examine O_2–$La_{0.5}Sr_{0.5}BO_{2.75}$ interactions. Results suggest that surface catalytic properties are strongly correlated with the bulk transport properties in several material systems with the formula of $La_{0.5}Sr_{0.5}BO_{2.75}$ (where B = Cr, Mn, Fe, or Co). The predictions seem to agree qualitatively with available experimental results on these materials. This computational screening technique may guide us to search for high-efficiency cathode materials for a new generation of SOFCs.

O_2 reduction mechanism on the cathode of an SOFC based on proton conductors [8]: While SOFCs based on oxide proton conductor BZCY electrolyte and mixed composite cathode might produce high and steady power densities at reduced temperatures. A composite cathode, consisting of $Ba(Zr_{0.1}Ce_{0.7}Y_{0.2})O_{3-\delta}$ (BZCY) and $La_{0.6}Sr_{0.4}Co_{0.2}Fe_{0.8}O_{3-\delta}$ (LSCF), demonstrated much-improved catalytic activity toward oxygen reduction than LSCF cathode. It appears that the addition of BZCY considerably increases the number of electrochemical reaction sites and expands them from the electrode/electrolyte interface to the entire surface of cathode.

Surface-Enhanced Raman Scattering (SERS) has used to study the surface of SOFC components in our group. We try to generate a SERS effect by incorporating silver or gold nano-particles onto a cathode surface using metal colloids and combustion chemical vapor deposition (CCVD). The overall spectrum intensity increased by up to one order of magnitude, but of particular interest in varying intensities of the peaks observed in the spectra collected from different locations. This use of the selected gold colloid did not cause any new peaks to emerge; all the peaks that were enhanced to different degrees could be found, albeit weakly, from the

untreated sample. These peaks are due to lattice modes and not from surface species, so the colloid did not seem to generate a signal from an individual surface species.

B. List of Publications/Presentations Resulting from the Grant (DE-FG02-06ER15837)

Refereed Journal Publications

1. Abernathy, H.W., E. Koep, C. Compson, Z. Cheng, and M.L. Liu, Monitoring Ag-Cr interactions in SOFC cathodes using Raman spectroscopy. Journal of Physical Chemistry C, 2008. 112(34): p. 13299-13303.
2. Yang, L., S.Z. Wang, K. Blinn, M.F. Liu, Z. Liu, Z. Cheng, and M.L. Liu, Enhanced Sulfur and Coking Tolerance of a Mixed Ion Conductor for SOFCs: BaZr0.1Ce0.7Y0.2-xYbxO3-delta. Science, 2009. 326(5949): p. 126-129.
3. Wang, J.H., Z. Cheng, J.L. Bredas, and M.L. Liu, Electronic and vibrational properties of nickel sulfides from first principles. Journal of Chemical Physics, 2007. 127(21): p. 214705.
4. Cheng, Z., H. Abernathy, and M.L. Liu, Raman spectroscopy of nickel sulfide Ni3S2. Journal of Physical Chemistry C, 2007. 111(49): p. 17997-18000.
5. Choi, S.H., J.H. Wang, Z. Cheng, and M. Liu, Surface modification of Ni-YSZ using niobium oxide for sulfur-tolerant anodes in solid oxide fuel cells. Journal of the Electrochemical Society, 2008. 155(5): p. B449-B454.
6. Wang, J.H. and M.L. Liu, Surface regeneration of sulfur-poisoned Ni surfaces under SOFC operation conditions predicted by first-principles-based thermodynamic calculations. Journal Of Power Sources, 2008. 176(1): p. 23-30.
7. Choi, Y.M., M.C. Lin, and M.L. Liu, Rational design of novel cathode materials in solid oxide fuel cells using first-principles simulations. Journal of Power Sources, 2010. 195(5): p. 1441-1445.
8. Yang, L., Z. Liu, S.Z. Wang, Y.M. Choi, C.D. Zuo, and M.L. Liu, A mixed proton, oxygen ion, and electron conducting cathode for SOFCs based on oxide proton conductors. Journal of Power Sources, 2010. 195(2): p. 471-474.
9. Choi, Y., M.C. Lin, and M.L. Liu, Computational study on the catalytic mechanism of oxygen reduction on La0.5Sr0.5MnO3 in solid oxide fuel cells. Angewandte Chemie-international Edition, 2007. 46(38): p. 7214-7219.
10. Choi, Y., D.S. Mebane, J.H. Wang, and M. Liu, Continuum and quantum-chemical modeling of oxygen reduction on the cathode in a solid oxide fuel cell. Topics in Catalysis, 2007. 46(3-4): p. 386-401.
11. Yang, L., C.D. Zuo, and M.L. Liu, High-performance anode-supported Solid Oxide Fuel Cells based on Ba(Zr0.1Ce0.7Y0.2)O3-delta (BZCY) fabricated by a modified co-pressing process. Journal Of Power Sources, 2010. 195(7): p. 1845-1848.
12. Yang, L., C.D. Zuo, S.Z. Wang, Z. Cheng, and M.L. Liu, A novel composite cathode for low-temperature SOFCs based on oxide proton conductors. Advanced Materials, 2008. 20(17): p. 3280.
13. Choi, Y.M., D.S. Mebane, M.C. Lin, and M.L. Liu, Oxygen reduction on LaMnO3-based cathode materials in solid oxide fuel cells. Chemistry of Materials, 2007. 19(7): p. 1690-1699.

14. Choi, Y.M., M.E. Lynch, M.C. Lin, and M.L. Liu, Prediction of O-2 Dissociation Kinetics on LaMnO3-Based Cathode Materials for Solid Oxide Fuel Cells. Journal of Physical Chemistry C, 2009. 113(17): p. 7290-7297.
15. Sepulveda, J., J.E. Wendler, R.E. Summons, and K.U. Hinrichs, Rapid Resurgence of Marine Productivity After the Cretaceous-Paleogene Mass Extinction. Science, 2009. 326(5949): p. 129-132.
16. Mebane, D.S., Y.J. Liu, and M.L. Liu, Refinement of the bulk defect model for LaxSr1-xMnO3 +/-delta. Solid State Ionics, 2008. 178(39-40): p. 1950-1957.
17. Lynch, M.E., D.S. Mebane, Y.J. Liu, and M.L. Liua, Triple-phase boundary and surface transport in mixed conducting patterned electrodes. Journal of the Electrochemical Society, 2008. 155(6): p. B635-B643.
18. Mebane, D.S., Y.J. Liu, and M.L. Liu, A two-dimensional model and numerical treatment for mixed conducting thin films. Journal of the Electrochemical Society, 2007. 154(5): p. A421-A426.

Invited and Contributed Presentations

1. M. Liu, "Understanding Interfacial Reactions in SOFCs – Modeling, Simulation, and In Situ Characterization", *Gordon Research Conference* on "High Temperature Materials", July 12-16, 2006.
2. M. Liu, H Abernathy, Y Choi, S Zha, Z Cheng, J Wang, R Das, E Koep, R Williams, and J Dong, "Recent Progress in Understanding Interfacial Reactions in SOFCs", *The 30th International Conference on Advanced Ceramics and Composites* (American Ceramic Society), Cocoa Beach, FL, January 2006.
3. H. T. Chen, Y. M. Choi, M. Liu, M. C. Lin, "Theoretical study of H_2S adsorption and decomposition on CeO_2(111) and defective CeO_{2-x}(111) surfaces," *231st American Chemical Society National Meeting*, Atlanta, GA, 2006.
4. H. Abernathy, Z. Cheng, X. Lou, M. Liu, "Probing and mapping SOFC anode reactions using in situ raman spectroscopy," *233rd American Chemical Society National Meeting*, Chicago, IL, United States, March 25-29, 2007.
5. H. Abernathy and M. Liu, "In situ Characterization SOFC Reactions Using Raman Spectroscopy", *Japan-US Frontier of Engineering*, Palo Alto, California, November 5-6, 2007.
6. M. Liu, "Recent Developments in Low-Temperature Solid Oxide Fuel Cells", Presented to *International Conference on Advanced Materials for Energy*", Barcelona, Spain, December 17-19, 2007.
7. Z. Cheng, S. Zha, H. Abernathy, M. Liu,"Experimental investigation of the sulfur poisoning process for solid oxide fuel cell anodes," *The 31s International Conference & Exposition on Advanced Ceramics & Composites*, Daytona Beach, Florida, 2007.
8. S. Choi, Y. M. Choi, C. Compson, M. C. Lin, M. Liu,"Investigation into sulfur tolerance of surface modified Ni anodes for solid oxide fuel cells," *Korea-USA Fuel Cell Symposium*, SC, 2007.
9. Y. M. Choi, M. C. Lin, M. Liu,"Computational studies of the oxygen reduction reaction on cathode materials for solid oxide fuel cells using quantum chemical calculations," *Korea-USA Fuel Cell Symposium*, SC, 2007.

10. S. Mebane, Y. Liu, M. Liu, "A Low-Temperature Defect Model for LaxSr1-xMnO3+/-delta," *European Ceramic Society Conference*, Berlin, Germany, 2007.
11. J. H. Wang, M. C. Lin, M. Liu,"Computational Study of Sulfur Poisoning of Ni under SOFC Operation Conditions by First-Principles and Thermodynamics," *Singapore International Chemistry Conference 5 & APCE Asia-Pacific International Symposium on Microscale Separation and Analysis*, Singapore, 2007.
12. J. H. Wang M. Liu, "Computational Study of Sulfur Poisoning and Surface Regeneration of Ni under SOFC Operation Conditions by First-Principles and Thermodynamics," The *31st International Cocoa Beach Conference*, Daytona Beach, Florida, 2007.
13. M. Liu, "Modeling and Simulation of Electrode Materials for SOFC", Presented to *International Conference on Clean Energy*, NRC, Vancouver, Canada, March 15, 2008.
14. M. Liu, "Recent Development in New Materials for Solid Oxide Fuel Cells", Presented to the *International Symposium on Renewable Energie*s South Korea, December 2-6, 2008.
15. M. Liu, "Modeling, Simulation, and In-situ Characterization of Electrode Materials for Solid Oxide Fuel Cells", Columbia University, New York, April 18, 2008.
16. M. Liu, "Functional Materials for Energy Storage and Conversion", Presented to the First International Symposium on Functional Metal Oxides, Ningbo Materials Research Institute, Chinese Academy of Sciences, Ningbo, China, December 16-20, 2008.
17. M. Liu, "Probing and Mapping Electrode Reactions using Raman Spectroscopy", University of West Virginia, Morgantown, WV, July 8, 2008.
18. M. Liu, "Modeling and Simulation of Composite Electrodes for SOFCs", Presented to *International Conference on Heterogeneous Materials*, in Huang-Shan, China, June 3-4, 2008.
19. M. Liu, "DFT Calculations of SOFC Materials", *DOE SECA Workshop on Cathode Materials for SOFCs*, Boston, MA, August 23, 2008.
20. M. Liu, "Modeling and Simulation of Electrode Materials for SOFC" Boston University, February 26, 2009.
21. M. Liu, "LSM Infiltrated LSCF Cathode" Carnegie Melon University, DOE-SECA Meeting, March 23-24, 2009.
22. M. Liu, "In-Situ Characterization of Electrode Processes Using Raman Spectroscopy", presented to *International Conference on Advanced Materials For Energy Applications*, Singapore, July 1, 2009.
23. M. Liu, "Rational Design of New Materials for Energy Storage and Conversion", Ulsan National Institute of Science and Technology (UNIST), South Korea, November 11, 2009.

C. Detailed Description of Significant Technical Progress

1. Identification of New Phases and Species on SOFC Electrode Surfaces

Raman spectroscopy has become a standard method for characterizing bulk materials, molecules, thin films, and surfaces.[1-12] Of the relatively few surface analysis methods available for *in situ* measurements, Raman spectroscopy is the most flexible in terms of having the largest window of operating conditions and the greatest range of surface species that can be probed and mapped.

Work performed in our lab has demonstrated the utility of Raman spectroscopy for studying various SOFC electrode materials and surface/interfacial processes, especially those involving oxygen,[3,4] sulfur,[5] carbon,[2] and hydrocarbons. In this project, we have demonstrated the utility of Raman spectroscopy for studying various SOFC electrode reactions. We have developed new methodologies for better understanding of the detailed catalytic mechanisms of electrochemical reactions in SOFCs. In particular, we has built a system for performing in situ Raman spectroscopy to probe and map new phases and species on electrode surfaces under fuel cell operating conditions, alongside electrochemical measurements to correlate with the electrochemical performance of the cell, as well as mass spectrometry to monitor the immediate chemical environment of an operating cell. [6] Briefly summarized below are some of our recent results using this technique

Figure 1 details results from a typical Cr contamination experiment, in which a patterned LSM cathode deposited on a YSZ substrate was exposed to Cr-containing vapor (humidified air blown over Cr_2O_3) at 625ºC for 24 hrs. Vapor phase chromium oxyhydroxides chemically reacted with the LSM, producing $SrCrO_4$ and $(Mn/Cr)_3O_4$. We are the first research group to produce *in situ* spectroscopic data directly observing the contaminating Cr-species as they form at high temperature, without possible error that accompanies conventional *ex situ* measurement due to reactions and phase changes during the sample cooling process. Chromium phases are not the only secondary phases that we have observed forming on the cathode. Cathodes with composition from the $La_{1-x}Sr_xCoO_3$ – $La_{1-x}Sr_xFeO_3$ system react with a YSZ electrolyte to form zirconate phases such as $La_2Zr_2O_7$ and $SrZrO_3$. Both of these phases are Raman-active.[10,11]

Figure 2 shows typical spectra collected from a micro-patterned Ni electrode on a YSZ substrate exposed to methane at 625ºC for 24 hrs. The SEM micrograph in Figure 2a reveals the presence of carbon spheroids on the Ni surface (the lighter region). We have also demonstrated the capability to monitor the deposition of carbon as a function of time, as shown in Figure 2b. The Raman map in Figure 2c shows the intensity of the 'G' band for carbon at 1580 cm^{-1} (associated with sp^2-bonded carbon). The carbon deposits cover the nickel surface almost entirely.

Shown in Figure 3(a) 13 is the observation of heazlewoodite (Ni_3S_2), millerite (NiS), polydymite (Ni_3S_4), and pyrite (NiS_2) were observed on Ni surface using Raman spectra, when the temperature was brought below 400^{o}C. These nickel sulfides decomposed to Ni and elemental sulfur upon heating up to higher temperatures, although the morphology of the Ni grains may have significantly changed as a result of the preceding reactions. In contrast, NbS_2 was detected on a Ni-YSZ anode coated with a thin film of NbO_2 after exposure to 100 ppm H_2S, as shown in Figure 3b. First principles calculations were used to confirm the peak assignments in these Raman spectra and the detailed vibrational modes in these sulfide compounds are listed in Table 1.[14] It is still not clear, however, why the formation of NbS_2 enhanced cell performance while the formation of nickel sulfides hindered it (i.e. a sulfur poisoning effect other than adsorbed sulfur blocking reaction sites). We can answer questions like this by resolving the relevant mechanism of interfacial processes from the first principles calculations based on periodic DFT and plane-wave basis set (1) to predict the reaction mechanisms of the gas-electrode interactions, (2) to estimate the intrinsic catalytic properties of SOFC materials, and (3) to provide fundamental knowledge for rational design of novel sulfur tolerant anodes. The information can

be used to uniquely identify each sulfide that may form in a given system, which would be critical to our proposed study.

Figure 4 shows Raman spectra collected from CeO_2 nanoparticles that had been treated in H_2 at 400ºC to clean the particle surface of undesired species (hydroxyls, carbonates). Following the surface cleaning with a room temperature exposure to oxygen caused the emergence of peaks at 831 and 1128 cm^{-1}, assigned to peroxide and superoxide species, respectively. The dioxygen nature of these two species were confirmed by repeating the experiment using the isotope $^{18}O_2$, causing the two peaks to shift to lower wave numbers (781 and 1064 cm^{-1}) due to the heavier oxygen atoms. Results from a similar experiment with $La_{0.5}Sr_{0.5}MnO_3$ (LSM) are shown in Fig. 4b. The surface of the LSM was cleaned by evacuated at 625ºC for 12 hrs, as LSM is not stable in a reducing H_2 atmosphere. Unlike the case of CeO_2, we were not able to detect a discernible surface oxygen signal from LSM. This result demonstrates the need for a way to increase the Raman signal intensity from species on a candidate electrode surface.

2. **New anode materials with excellent tolerance to coking and H_2S poisoning**

We have developed a new material for SOFCs that shows excellent tolerance to coking and H_2S poisoning. First, the new material displays the highest ionic conductivity below 750ºC among all SOFC electrolyte materials ever reported, thus allowing fabrication of anode-supported thin-electrolyte SOFCs of high power output at lower temperatures. Second, it exhibits exceptional tolerance to sulfur poisoning – there is no observable change in power output when the fuel is switched to one contaminated with H_2S, which is attributed to its excellent catalytic activity for conversion of H_2S to SO_2. Third, it displays significant activity for *in situ* reforming of hydrocarbon fuels, which minimizes the tendency of coking. Finally, it demonstrates adequate chemical and electrochemical stability over a wide range of conditions relevant to SOFC operation, implying long-term stability and long operational life. We have systematically investigated this material as the anode in H_2S-contaminated H_2 and hydrocarbon fuels. The test cells displayed not only impressive power output in clean hydrogen but also superior tolerance to coking and sulfur poisoning. The new material has great potential to dramatically improve the economical competitiveness and commercial viability of SOFCs that are driven by cost-effective and renewable fuels.

Shown in Figure 5A is the terminal voltages of the Ni-BZCYYB supported cells (with BZCYYb and SDC as the electrolyte) at 750°C were recorded as a function of time when the fuel was contaminated with different concentrations of H_2S. The Ni-BZCYYb anodes for both cells showed no observable change in power output as the fuel was switched from clean hydrogen to hydrogen contaminated with 10, 20, or 30 ppm H_2S. This sulfur tolerance was also evident from our impedance data (Figure 5 B and C). When water was absent from the fuel, the electrode polarization resistance increased about 80% upon exposure to 20 ppm H_2S, from ~0.06 ohm·cm^2 in H_2 to ~0.11 ohm·cm^2 in H_2 containing 20 ppm H_2S, as commonly observed in previous studies[5]. When a small amount of water (only ~3 vol %) was introduced with the fuel, the electrode polarization resistance in hydrogen with 20 ppm H_2S was reduced to that in clean hydrogen, as can be interpreted from the collected impedance spectra (Figure 5C). It is believed that sulfur poisoning is caused by the strong adsorption of the elemental sulfur on Ni surface and the three-phase boundaries (TPBs) between Ni, electrolyte, and the fuel. Sulfur would then block

the active site for fuel oxidation in a traditional Ni-YSZ anode and increase the polarization resistance[13]. We hypothesized that water might adsorb on the surface of BZCYYb to facilitate the oxidation of H_2S or elemental sulfur to SO_2 at or near the active sites. Unlike H_2S or elemental sulfur, SO_2 readily desorbs from electrode surface [14]. When the fuel was switched to hydrogen containing 40 and 50 ppm H_2S, the cell with a BZCYYb electrolyte (a mixed proton and oxide ion conductor) suffered some drop in power output, whereas the cell with an SDC electrolyte (an oxide ion conductor) displayed no observable change in performance. One possible explanation is that more water was produced at the active sites on the anode of the cell with an SDC electrolyte under active operation because of increased hydrogen oxidation; the water produced at the active sites is beneficial to sulfur removal. Continuous operation in H_2S-contaminated fuel for a longer period of time (200 to 1000 hours) further confirmed that sulfur poisoning can be fully suppressed in the presence of a small amount of steam.

Shown in Figure 6 is the coking resistance demonstrated in a cell with a Ni-BZCYYb cermet anode, YSZ electrolyte, and LSCF cathode. When dry propane was used as fuel, the OCV dropped quickly within minutes, an indication of rapid carbon deposition as expected for a conventional Ni-based anode. In contrast, when wet (~3 vol % steam) propane was used as fuel, the OCV was very stable, suggesting that the observed tolerance to coking is also attributed to the presence of a small amount of steam. Further, the contamination of Ni surface by BZCYYb during co-firing of BZCYYb and NiO might enhance the resistance to carbon buildup. The whole surface of the Ni-BZCYYb anode exposed to wet (~3 vol % H_2O) propane appeared clean and free of carbon deposition, as revealed by Raman spectroscopy[15]. The OCVs of the cell are greater than those observed for other alternative anode materials [16-19] and approach 1.00 V for wet propane. Coking may be inhibited by water reforming propane on the surface of BZCYYb, and the reforming products (H_2 and CO) adsorb on the active sites of the anode surface, leading to a stable OCV output. We note that conventional Ni-YSZ and Ni-GDC anodes suffered severe carbon deposition under the same conditions.

3. Rational design of cathode materials for SOFC using first-principles simulations

Here we report our results on a computational study to achieve rational design of SOFC cathodes with fast oxygen reduction kinetics and rapid ionic transport. Results suggest that surface catalytic properties are strongly correlated with the bulk transport properties in several material systems with the formula of La0.5Sr0.5BO2.75 (where B = Cr, Mn, Fe, or Co). The predictions seem to agree qualitatively with available experimental results on these materials. This computational screening technique may guide us to search for high-efficiency cathode materials for a new generation of SOFCs.

Shown in Figure 7a is the 2D slab-model calculations based on the four-layer (1 0 0) surfaces to examine O_2–$La_{0.5}Sr_{0.5}BO_{2.75}$ interactions.. A vacuum space with 24 Å in the perpendicular direction to the surface was used to guarantee no interactions between slabs. All surface calculations were performed by relaxing the top two layers while fixing the bottom two layers to the estimated bulk parameters. The relative energies for the O_2-surface interactions are calculated according to $\Delta E_{ads} = E_P - E_R$, where E_P and E_R are the calculated energies of products and reactants, respectively. Illustrated in Figure 7b are energetically the most plausible configurations, including molecular adsorption, dissociation, and incorporation into an oxygen

vacancy. Further, Figure 7c clearly shows that the adsorption energies of adsorbed species (e.g., molecular adsorption, dissociation, and incorporation processes) are well correlated with the B cations in the four Sr-doped $LaBO_3$ cathodes. This means that the bond strength between B cation and O atom may be a crucial indication of catalytic activity toward oxygen reduction for charge transfer from d orbital of B cations to 2p orbital of molecular oxygen [20]. Cr-based MIEC cathodes have the strongest bond with adsorbed oxygen species. However, regarding surface exchange coefficients associated with a surface catalytic activity toward oxygen reduction,LSC50 has a much faster O_2 kinetics than LSM50 [21] and[22]. Although one has to take into account other parameters (e.g., the concentrations of oxygen vacancies, electrons, and electron holes) [23] to estimate surface oxygen exchange coefficients, the trend shown in Figure 7c seems to suggest that the adsorption-energy calculations are reasonably related to the catalytic activity toward oxygen reduction. Compared with the parameters determined from SIMS [21] and [22], our DFT calculations verify that LSC-based MIEC cathodes have the highest catalytic activity. Furthermore, Figure 7d manifests that the surface diffusion of adsorbed oxygen species after dissociation also have a strong relevance to the B cations, indicating that the bond strength between surfaces and oxygen species becomes weaker as Z increases. This may mean that the adsorbed oxygen species or oxygen ions after dissociation/incorporation processes, respectively, on LSC50 can more easily diffuse on the surface or to the TPB compared to others. In addition, on the basis of the estimation of the bulk-diffusion barriers (E_a) of oxygen ions through the MIEC bulk phases and the adsorption energies , we examined their correlation as shown in Figure 8. The four cathodes materials ($La_{0.5}Sr_{0.5}CrO_{2.75}$, LSCr50; $La_{0.5}Sr_{0.5}MnO_{2.75}$, LSM50; $La_{0.5}Sr_{0.5}FeO_{2.75}$**,** LSF50; $La_{0.5}Sr_{0.5}CoO_{2.75}$, LSC50**)** show a very good correlation with a slight deviation of LSM50.

Shown in figure 8 is the effect of A cation substitution by replacing La with Ce, Pr, Nd, Pm, and Sm ($Ce_{0.5}Sr_{0.5}MnO_{2.75}$,CeSM50; $Pr_{0.5}Sr_{0.5}MnO_{2.75}$, PrSM50; $Nd_{0.5}Sr_{0.5}MnO_{2.75}$, NdSM50; $Pm_{0.5}Sr_{0.5}MnO_{2.75}$, PmSM50; $Sm_{0.5}Sr_{0.5}MnO_{2.75}$,SSM50, respectively. Interestingly, only SSM50 have a much closer character to LSC50, implying that Sm may play a role in exhibiting a higher catalytic activity toward oxygen reduction and a lower diffusion barrier. Our further examination of $Sm_{0.5}Sr_{0.5}CoO_{2.75}$ (SSC50**)** and $Sm_{0.5}Sr_{0.5}FeO_{2.75}$ (SSF50) verifies the Sm effect. It is noted that our prediction of the activation barrier of SSC50 is in excellent agreement with the experimental value (1.1 eV vs. 0.9 eV) [24]. Thus, figure 8 manifests that the adsorption energies of oxygen species have a strong correlation with the diffusion barriers of oxygen ion transport. Comparison with cathode materials that are known catalytically active at low temperatures (LSC and SSC) suggests that tailoring novel cathode materials must also consider the need for a weak binding between a surface and oxygen species with a low O-diffusion barrier, although other factors (such as thermal mismatch with the electrolyte materials) have to be considered as well. We will extend our simulations to more realistic surface models$(A_{1-x}A'_x)(B_{1-y}B'_y)O_{3-\delta}$ (i.e., A = La or Sm, A′ = Sr, B = Co, B′ = Fe or Mn) to predict the effect of defects and other relevant conditions on surface catalytic and ionic transport properties.

4. Composite cathode materials for SOFCs based on oxide proton conductors

It is well known that mixed ionic and electronic conducting (MIEC) cathode on an oxygen ion conducting electrolyte could expand the electrochemically active reaction sites from the triple phase boundary (TPB) to the cathode surface, as shown in Figure 9(a). However, when applying

an MIEC on a proton conducting electrolyte, the oxygen reduction can only take place at the interface where electrode, electrolyte, and the gas phase are in contact and where the access to oxygen, proton, and electrons are met for the reduction reaction as indicated in Figure 9(b). The limited reaction sites may lead to large electrode polarization resistance. This could explain why pure SSC cathode exhibits poor electrochemical performance (an overpotential of 350 mV at a current density of 100 mA cm^{-2} at 600 °C) on Y-doped barium cerate electrolyte [25]. In order to expand reaction zone beyond the interface, a potential cathode material must be able to conduct proton, oxygen ions and electrons. A mixed proton, oxide ion and electron conducting cathode extends the TPB from the interface to the entire cathode, thereby greatly accelerating the charge transfer reaction. From these points of view, a fuel cell based on proton conducting electrolyte using this mixed conducting cathode should reduce the resistance to oxygen reduction reactions. Unfortunately, a single-phase proton, oxygen ion and electron conductor with significant electronic conductivity is not yet developed [25]. Thus, a composite cathode consisting of a proton conductor and a mixed oxygen ion and electron conductor (MIEC) may facilitate simultaneous transport of proton, oxide ion, and electron for the oxygen reduction, as schematically shown in Figure 9 (c). The other advantage of this concept is that well-developed MIECs can be mixed with a proton conductor to tailor the properties. In this study, LSCF was mixed with BZCY to form a composite cathode that transport proton, oxide ion, and electron, exhibiting very low polarization resistance and high power density.

As shown in Figure 10(a) is the dependence of cell voltages and power densities on cell operating current densities at different temperatures for BZCY-based fuel cells using BZCY–LSCF and LSCF cathodes. The open circle voltages (OCV) at 750, 650, and 550 °C are 1.01, 1.06, and 1.11 V, respectively. This indicates that the BZCY electrolyte is sufficiently dense and exhibits negligibly small electronic conduction. More importantly, BZCY–LSCF composite cathode produced much higher power output than the LSCF cathode under the same operating conditions. The peak power densities were 855, 522, and 215 mW cm^{-2} at 750, 650, and 550 °C, respectively. These performances are surprisingly high for a cell based on a 55 μm thick electrolyte, even better than that based on an oxygen ion conductor (e.g., 26 μm thick GDC electrolyte and GDC–SSC cathode showed 330 and 205 mW cm^{-2} at 650 and 550 °C, respectively) [26]. In contrast, the cell with the LSCF cathode displayed 435, 235, and 81 mW cm^{-2} at 750, 650, and 550 °C, respectively. Figure 10(b) summarizes the polarization resistances of typical cells with BZCY–LSCF and LSCF cathodes measured at different temperatures. Obviously, BZCY–LSCF exhibits much lower cathodic polarization resistances than the LSCF cathode in all cases. The polarization resistances of cells with BZCY–LSCF are estimated to be only 0.19, 0.47, and 1.34 Ω cm^2 at 650, 600, and 550 °C, respectively, comparable to those of the GDC–LSCF composite cathode on GDC electrolyte (0.13, 0.33, and 1.24 Ω cm^2 at 650, 600, and 550 °C, respectively), as shown in Figure 10(c) . SEM examination of fresh BZCY–LSCF and LSCF cathodes reveals that their surface and cross-sectional morphologies are very similar, suggesting that the remarkable improvement in performance is due primarily to the superior catalytic activity of BZCY–LSCF cathode.

5. Surface-enhanced Raman spectroscopy (SERS)

The presence of metal nano-particles (usually silver or gold) has been found to enhance the Raman scattering efficiency of the surrounding area on the order of 10^6 [27,28] The bulk of the

enhancement is thought to derive from the interaction of the surface species with a plasmon field generated around the metal nanoparticles in the presence of the laser's electromagnetic field.[29,30] The key to the enhancement factor is the size and curvature of the nanoparticle, as well as the orientation of the species with respect to the plasmon field. Today, within certain systems, Raman enhancement factors as high as 10^{31} have been obtained for single molecules, allowing for their isolation and detection.[32] The enhancement effect quickly decays within a few nanometers from the nanoparticle, so it is an ideal technique for observing surface species and surface structures. Many factors such as the temperature, the laser excitation wavelength, and the nature of the sample ultimately control the amount of Raman enhancement available through SERS, so no standardized method currently exists for all applications.[33] Instead, a methodology must be tailored for each specific application.

SERS signals are typically generated from molecules adsorbed to the surface of a metal nanoparticle. While this signal is difficult to avoid, our main concern is the SERS signal from surface molecules and thin films located within a few nanometers of the particle. While this concept is untraditional, it is not without precedent. Huang *et al.* have reported using SERS to see thin Nb-O films located underneath SERS-active particles.[34]

To date, there are no published literature reports of any attempts to use SERS to study the surface of SOFC components; however, our research group has made some initial attempts to generate a SERS effect by incorporating silver or gold nanoparticles onto a cathode surface using metal colloids and combustion chemical vapor deposition (CCVD). Figure 11(a) shows Raman spectra collected from the surface of a dense SSC pellet to which two drops of a 20 nm gold colloid had been applied and allowed to dry. The overall spectrum intensity increased by up to one order of magnitude, but of particular interest in varying intensities of the peaks observed in the spectra collected from different locations. The 513, 684, and 780 cm^{-1} peaks received large, but not uniform enhancements. This use of the selected gold colloid did not cause any new peaks to emerge; all the peaks that were enhanced to different degrees could be found, albeit weakly, from the untreated sample. These peaks are due to lattice modes and not from surface species, so the colloid did not seem to generate a signal from an individual surface species.

Shown in Figure 11b are the Raman spectra from $Sr_{0.5}Sm_{0.5}CoO_3$ in air before and after application of Ag colloid with heat treatment at 325°C. While the conventional Raman spectrum is largely featureless, 15-20 new peaks emerge in the SERS spectrum. Some of the peaks in the 800-1100 cm^{-1} range likely correspond to peroxide and superoxide species adsorbed on the SSC surface, whereas the large peak near 1500 cm^{-1} can possibly be attributed to neutral surface oxygen molecules. The rest of the peaks may indicate other surface contaminants. Clearly, the SERS methodology has shown significant promise in characterizing of the surface structure and chemistry of SOFC electrodes. In addition to incorporating Ag and Au nanoparticles from colloids, we have also made our SOFC electrode materials SERS-active by short-term DC sputtering of Ag on the materials and by co-deposition of the materials with Ag nanoparticles by combustion chemical vapor deposition (CCVD). Raman spectra collected from the SERS-active materials (e.g., LSM, LSC, SSC, and LSCF) showed enhancement of more than one order of magnitude for peaks corresponding to lattice phonon modes and surface adsorbed oxygen species, demonstrating that SERS is a powerful tool for in situ characterization of surface structure and chemistry of electrode materials.

References

(1) Mestl, G. *J Mol Catal A-chem* **2000**, *158*, 45.
(2) M. A. Banares, R. S., " in In Situ Spectroscopy of Catalysts, B. M. Weckhuysen, Ed. USA: American Scientific Publishers, p. 332. (2004).
(3) Choi, Y. M.; Abernathy, H.; Chen, H. T.; Lin, M. C.; Liu, M. L. *Chemphyschem* **2006**, *7*, 1957.
(4) Pushkarev, V. V.; Kovalchuk, V. I.; d'Itri, J. L. *Journal of Physical Chemistry B* **2004**, *108*, 5341.
(5) Cheng, Z.; Liu, M. L. *Solid State Ionics* **2007**, *178*, 925.
(6) Yang, H. Z.; Yang, Y. Q.; Zou, S. Z. *Journal of Physical Chemistry B* **2006**, *110*, 17296.
(7) Abernathy, H. W.; Koep, E.; Compson, C.; Cheng, Z.; Liu, M. L. *J. Phys. Chem. C* **2008**, *112*, 13299.
(8) Iliev, M. N.; Litvinchuk, A. P.; Abrashev, M. V.; Ivanov, V. G.; Lee, H. G.; McCarroll, W. H.; Greenblatt, M.; Meng, R. L.; Chu, C. W. *Physica C* **2000**, *341*, 2257.
(9) Venimadhav, A.; Yates, K. A.; Blamire, M. G. *J Comb Chem* **2005**, *7*, 85.
(10) Fujimori, H.; Kakihana, M.; Ioku, K.; Goto, S.; Yoshimura, M. *Journal of the Ceramic Society of Japan* **2004**, *112*, 189.
(11) Shimamura, K.; Arima, T.; Idemitsu, K.; Inagaki, Y. *International Journal of Thermophysics* **2007**, *28*, 1074.
(12) R. J. Nemanich, J. T. G., G. Lucovsky, and R. E. Shroder, "Raman-scattering characterizion of carbon bonding in diamond and diamondlike thin-films," Journal of Vacuum Science & Technology a-Vacuum Surfaces and Films, 6, 1783-1787, (1988).
(13) Wang, J. H.; Liu, M. L. *Electrochemistry Communications* **2007**, *9*, 2212.
(14) Wang, J. H.; Liu, M. L. *J Power Sources* **2008**, *176*, 23.
(15) Yang, L.; Wang, S. Z.; Blinn, K.; Liu, M. F.; Liu, Z.; Cheng, Z.; Liu, M. L. *Science* **2009**, *326*, 126.
(16) Park, S. D.; Vohs, J. M.; Gorte, R. J. *Nature* **2000**, *404*, 265.
(17) Tao, S. W.; Irvine, J. T. S. *Nature Materials* **2003**, *2*, 320.
(18) Huang, Y. H.; Dass, R. I.; Xing, Z. L.; Goodenough, J. B. *Science* **2006**, *312*, 254.
(19) Mogensen, M.; Kammer, K. *Annual Review of Materials Research* **2003**, *33*, 321.
(20) Choi, Y.; Lin, M. C.; Liu, M. L. *Angew Chem Int Edit* **2007**, *46*, 7214.
(21) De Souza, R. A.; Kilner, J. A. *Solid State Ionics* **1998**, *106*, 175.
(22) De Souza, R. A.; Kilner, J. A. *Solid State Ionics* **1999**, *126*, 153.
(23) De Souza, R. A. *Physical Chemistry Chemical Physics* **2006**, *8*, 890.
(24) I.C. Fullarton, J. A. K., B.C.H. Steele and P.H. Middleton In: T.A. Ramanarayanan, W.L. Worrell and H.L. Tuller, Editors, Proceedings of the 2nd International Symposium on Ionic and Mixed Conducting Ceramics, vol. 94-12, Electrochemical Society, Pennington, NJ (1994), pp. 9–26.
(25) Hibino, T.; Hashimoto, A.; Suzuki, M.; Sano, M. *Journal of the Electrochemical Society* **2002**, *149*, A1503.
(26) Xia, C. R.; Liu, M. L. *Solid State Ionics* **2001**, *144*, 249.
(27) Nikoobakht, B.; El-Sayed, M. A. *Journal of Physical Chemistry A* **2003**, *107*, 3372.
(28) K. Kneipp, M. M., and H. Kneipp, Surface-enhanced raman scattering : physics and applications vol. 103. New York: Springer, (2006).
(29) E. Smith and G. Dent, M. R. S. A. P. A. H., NJ: Wiley, (2005).

(30) R. Aroca, S. E. V. S. H., NJ: Wiley, (2006).
(31) Schwan, J.; Ulrich, S.; Batori, V.; Ehrhardt, H.; Silva, S. R. P. *Journal of Applied Physics* **1996**, *80*, 440.
(32) Nie, S. M.; Emery, S. R. *Science* **1997**, *275*, 1102.
(33) Hering, K.; Cialla, D.; Ackermann, K.; Dorfer, T.; Moller, R.; Schneidewind, H.; Mattheis, R.; Fritzsche, W.; Rosch, P.; Popp, J. *Analytical and Bioanalytical Chemistry* **2008**, *390*, 113.
(34) Huang, B. X.; Wang, K.; Church, J. S.; Li, Y. S. *Electrochimica Acta* **1999**, *44*, 2571.

Figures

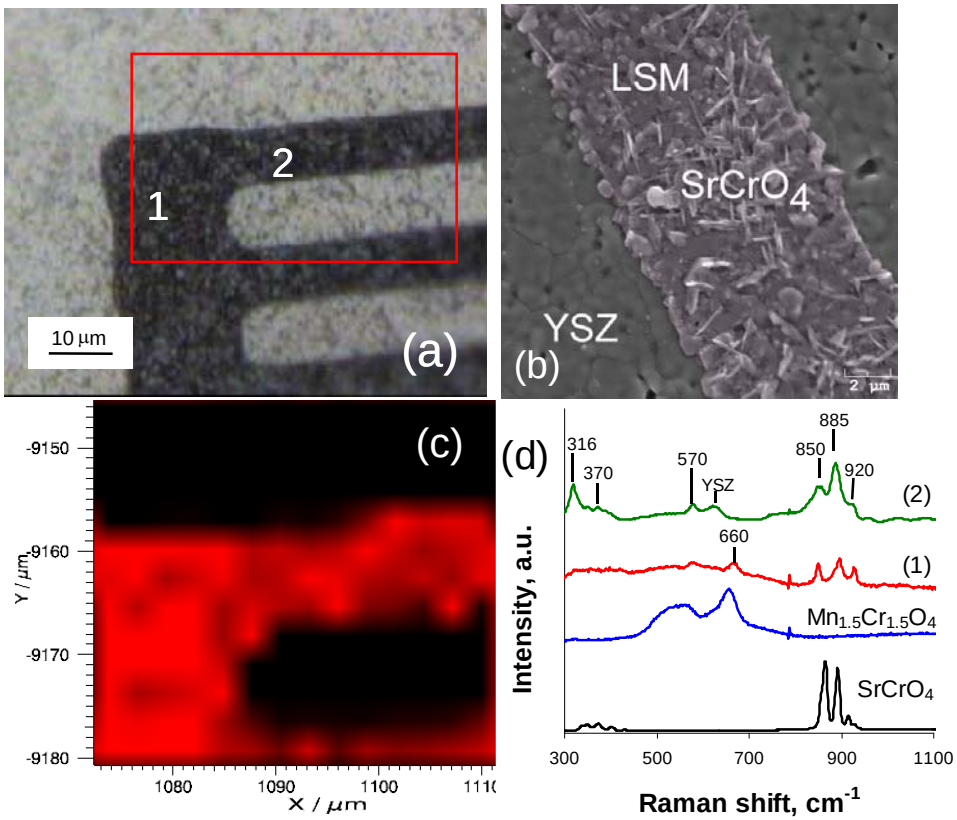

Figure 1. (a) Optical micrograph and (b) SEM image of a patterned LSM cathode (on YSZ) exposed to Cr-containing vapor at 625ºC for 24 hrs. The Raman map (c) from the area indicated in (a) shows the intensity variation of the 885 cm^{-1} $SrCrO_4$ peak seen in the reference Raman spectrum shown in (d). Spectra (1) and (2) are from the points indicated in (a).

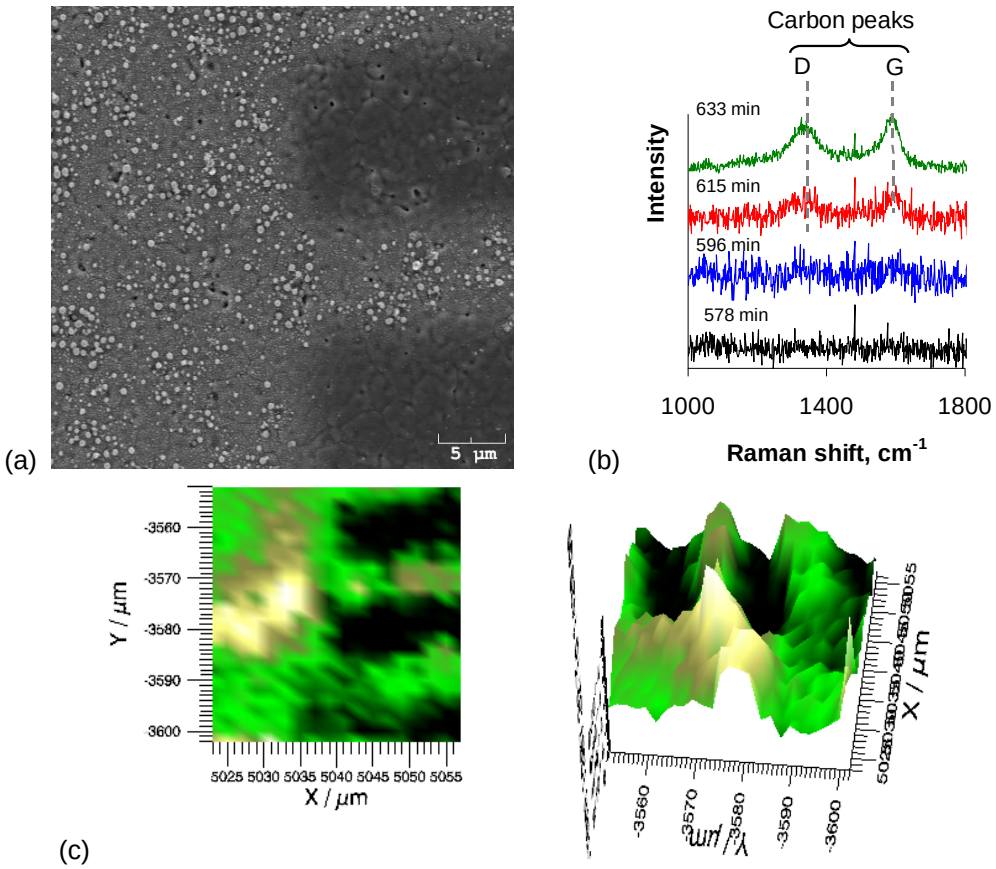

Figure 2. A study of carbon deposition on a patterned Ni anode on a YSZ substrate exposed to CH_4 at 625ºC. (a) SEM micrograph showing carbon particles on the Ni surface (the lighter phase) after 24 hrs exposure to CH_4. (b) Raman spectra collected from the Ni surface as a function of time. (c) Raman map of the 1580 cm^{-1} carbon peak. A lighter shade indicates higher peak intensity.

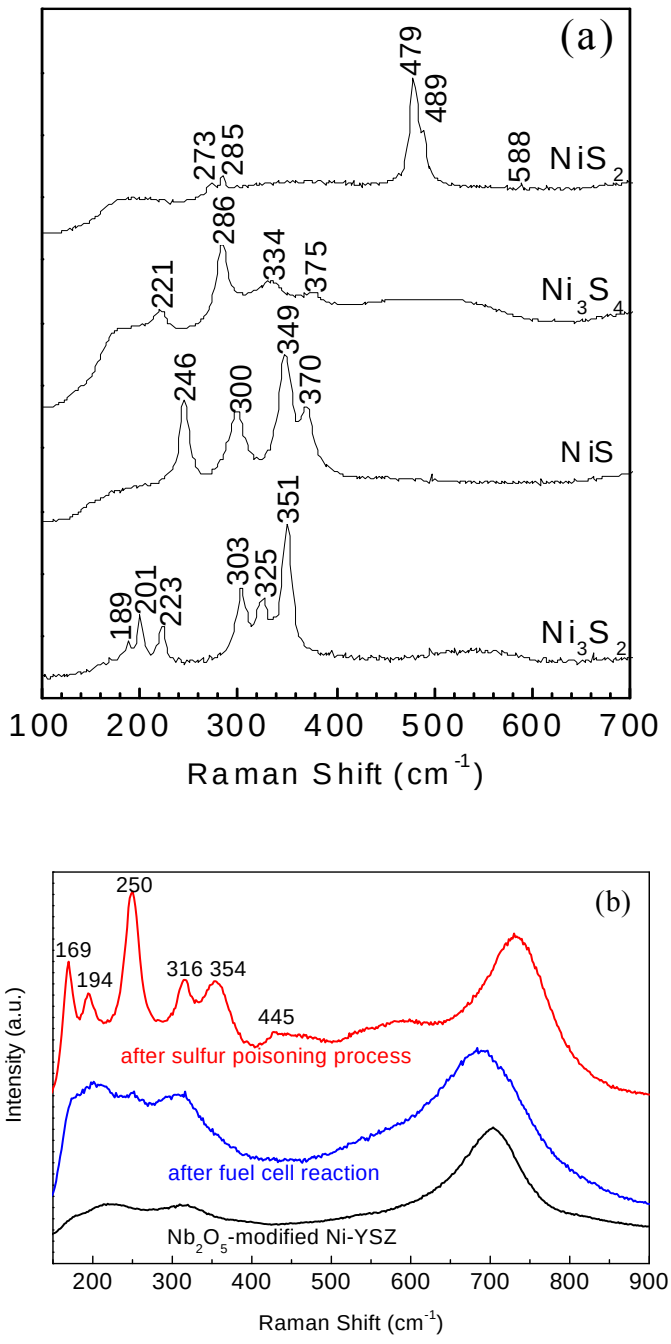

Sulfide	Modes	Calc.	Expt.
Ni_3S_2	E(1)	367, 367	351
	A_1(1)	320	325
	E(2)	317, 316	303
	E(3)	241, 241	223
	E(4)	204, 203	201
	A_1(2)	201	189
NiS	A_1(1)	356	370
	E(1)	341, 341	349
	A_1(2)	290	300
	A_1(3)	254	
	E(2)	252, 251	246
	E(3)	231, 230	226
	E(4)	201, 201	172
	E(5)	148, 148	151
Ni_3S_4	A_{1g}(1)	388	375
	T_{2g}(1)	339, 338, 338	335
	T_{2g}(2)	284, 284, 283	285
	E_g(1)	208, 207	222
	T_{2g}(3)	206, 206, 205	208
NiS_2	T_g(1)	462, 462, 461	489
	A_g(1)	446	479
	T_g(2)	342, 341, 341	
	E_g(1)	285, 285	285
	T_g(3)	278, 278, 277	273
NbS_2	E(1)	394, 393	445
	A_1(1)	389	
	E(2)	349, 349	354
	A_1(2)	329	316
	E(3)	249	
	E(4)	244, 243	250
	A_1(3)	243	
	E(5)	205, 205	194
	E(6)	203, 203	
	E(7)	183, 183	169

Figure 3: Raman spectra collected under *in situ* conditions from (a) a Ni-YSZ anode and (b) an Nb_2O_5-coated Ni-YSZ anode exposed to H_2S-contaminated hydrogen. **Table**: Calculated and experimentally observed Raman frequencies of the sulfides.

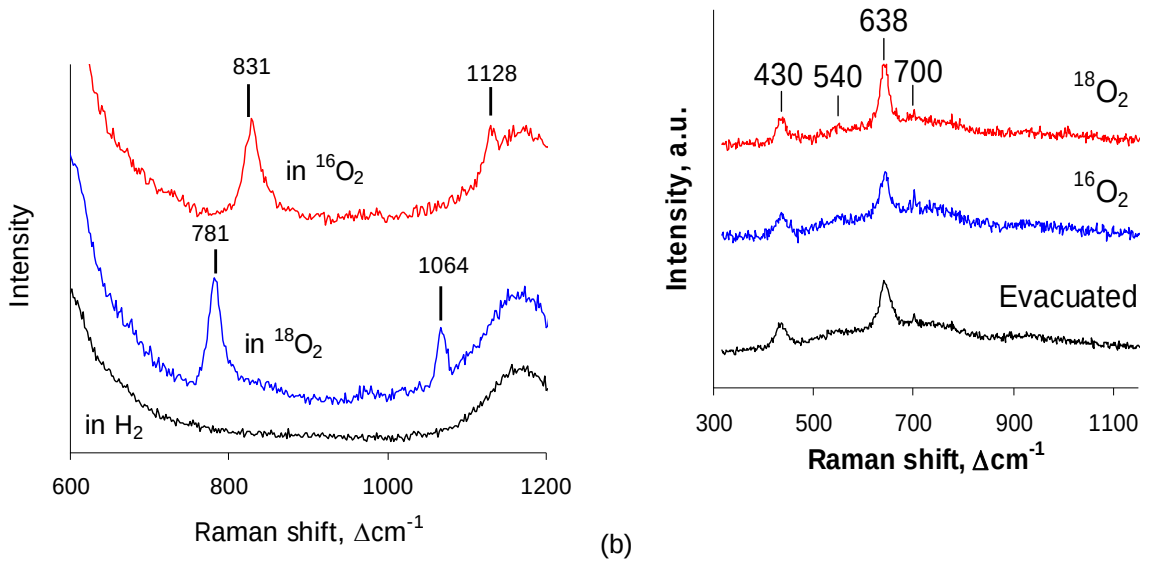

Figure 4. (a) Raman spectra from CeO_2 nanoparticles treated in 10% H_2 at 400ºC before exposure to at room temperature to either 100% $^{16}O_2$ or $^{18}O_2$. (b) Raman spectra from $La_{0.5}Sr_{0.5}MnO_3$ after evacuation at 625ºC, followed by exposure to $^{16}O_2$ or $^{18}O_2$.

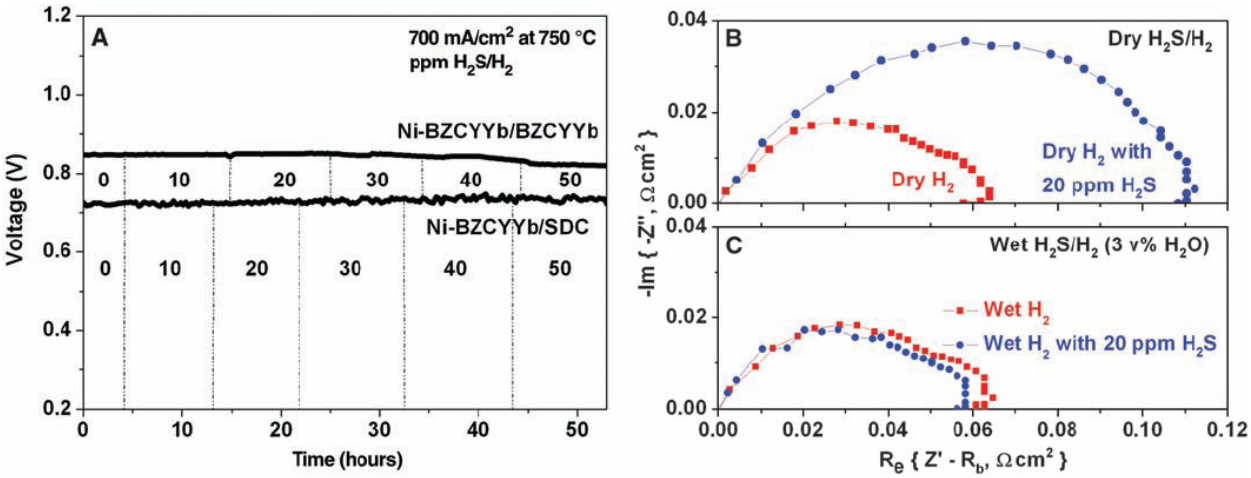

Figure 5. Terminal voltages measured at 750°C as a function of time for two cells with a configuration of Ni-BZCYYb | BZCYYb | BZCY-LSCF and Ni-BZCYYb | SDC | LSCF operated at a constant current density of 700 mA/cm2 as the fuel was switched from clean H2 to H2 contaminated with different concentrations of H2S (the number in each time interval represents the concentration of H2S in wet hydrogen in ppm).

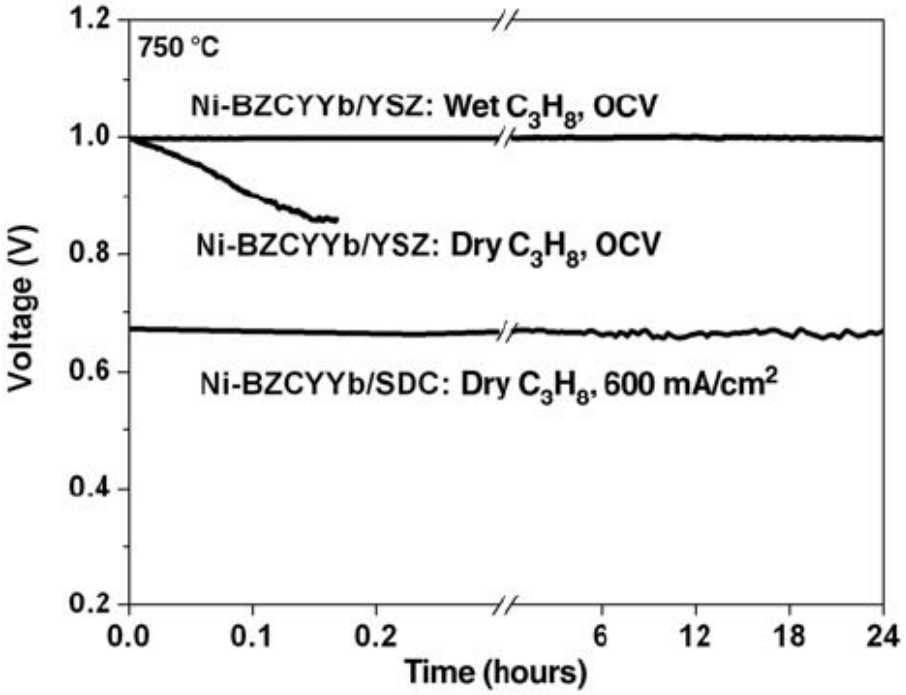

Figure 6. Open cell voltages measured at 750°C as a function of time for a cell with a configuration of Ni-BZCYYb | YSZ | LSCF with dry and wet propane as the fuel, and the terminal voltages for another cell with a configuration of Ni-BZCYYb | SDC | LSCF operated at 600 mA/cm2 using dry propane as fuel. Stationary air was used as oxidant in all cases.

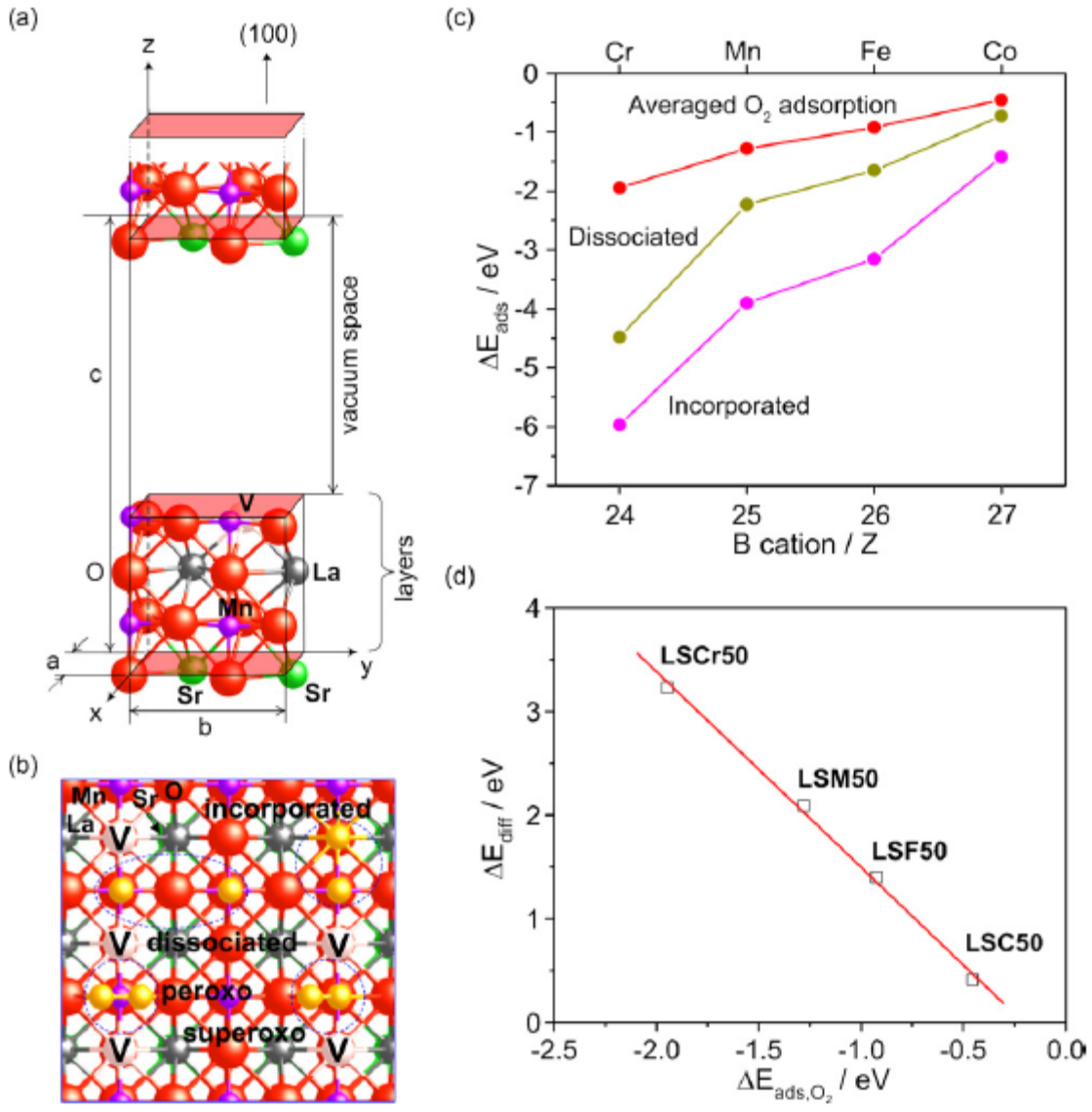

Figure 7 (a). representative surface model with four layers for the interactions between oxygen species and La0.5Sr0.5MnO2.75. (b) The species in dashed circles are surface oxygen species formed via adsorption or incorporation into oxygen vacancies. V denotes an oxygen vacancy. (c).Adsorption energies of surface oxygen species versus B cations. Averaged O_2 adsorption corresponds to averaged adsorption energies of superoxo- and peroxo-like species. "Dissociated" denotes the adsorption energies of two dissociated oxygen species, while and "Incorporated" is that one of dissociated oxygen species is incorporated into an oxygen vacancy. (d)A correlation between surface diffusion barriers of adsorbed O species on B cations (ΔE_{diff}) and averaged O_2 adsorption energies on four Sr-doped $LaBO_{2.75}$ surfaces.

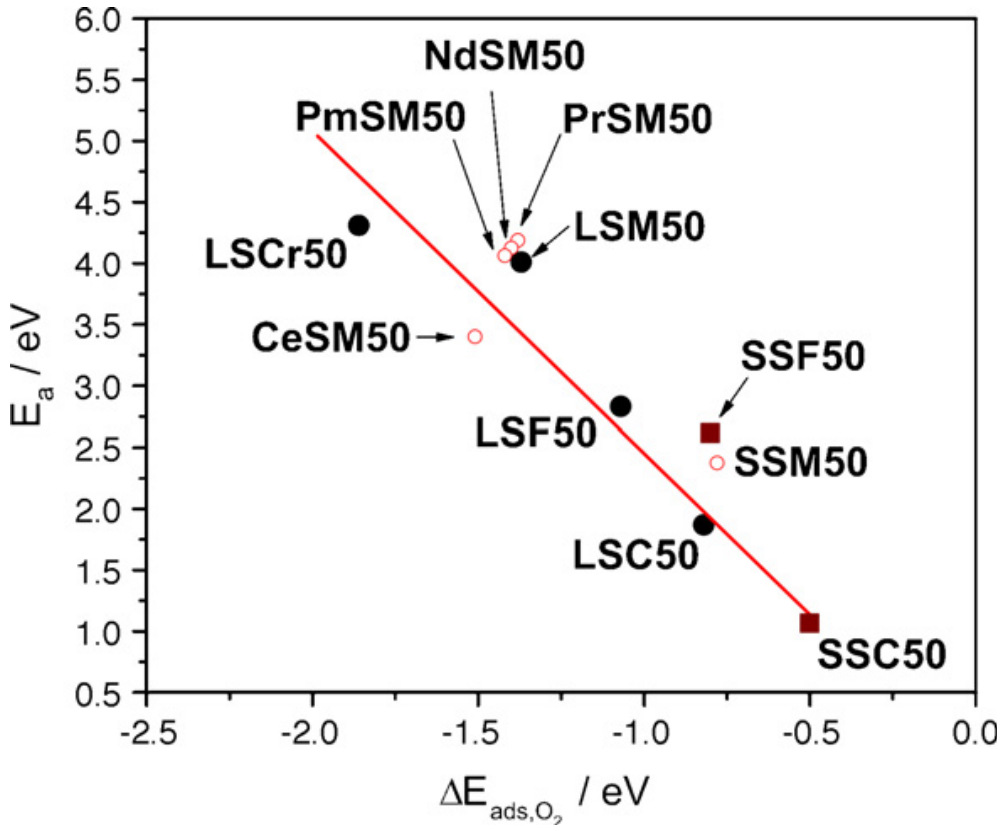

Figure 8. Comparison of adsorption energies versus diffusion barriers of oxygen ions through the MIEC bulk phases. Ea denotes the diffusion barriers of oxygen ion transport through the bulk MIEC phases, while _Eads,O2 is the averaged adsorption energies of superoxo- and peroxo-like species on B cations. The linear line in red was obtained from LSCr50, LSM50, LSF50, and LSC50.

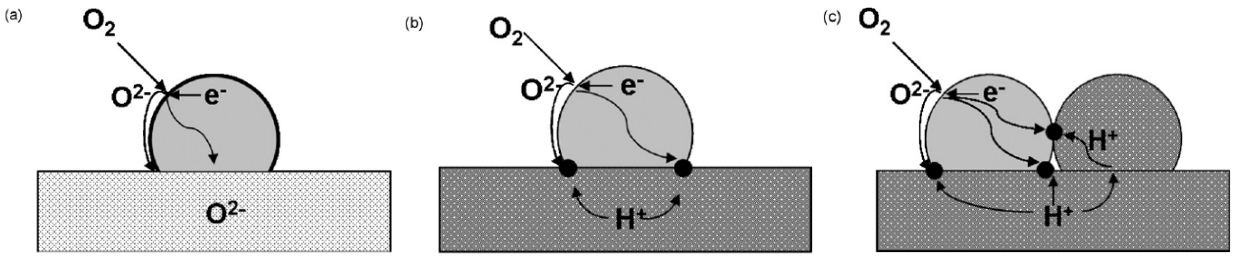

Figure 9. Schematic illustration of oxygen reduction reaction sites (a) a mixed oxygen ion–electron conducting cathode on oxygen ion conducting electrolyte; (b) a mixed oxygen ion–electron conducting cathode on a proton conducting electrolyte, and (c) a mixed proton–oxygen ion–electron conducting cathode on a proton conducting electrolyte. The circles denote electrochemically active reaction sites.

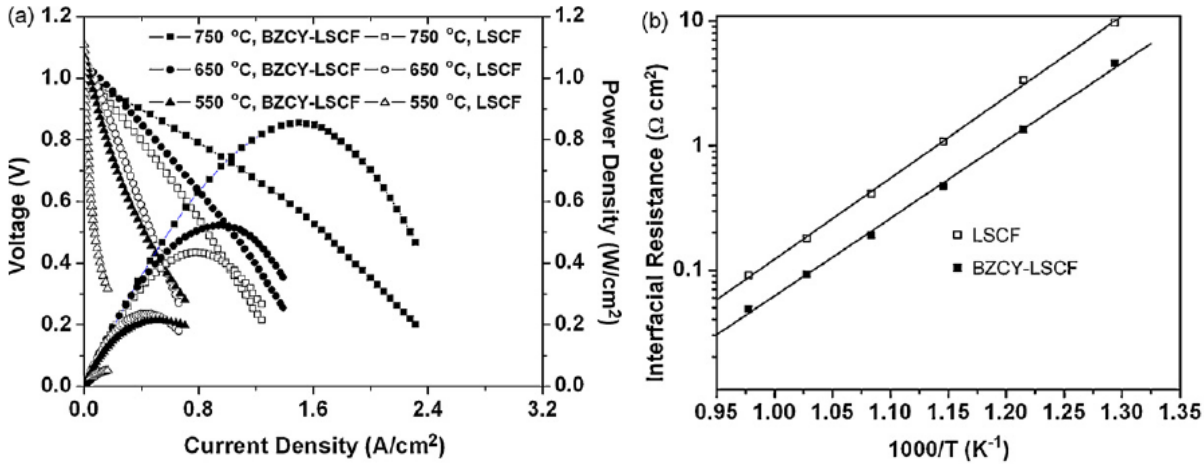

Figure 10. (a) *V–I* characteristics for BZCY-based anode-supported cells with BZCY–LSCF and LSCF cathodes as measured in humidified (3% H_2O) H_2 at 550–750 °C; (b) polarization resistances of the cells with LSCF and BZCY–LSCF cathode.

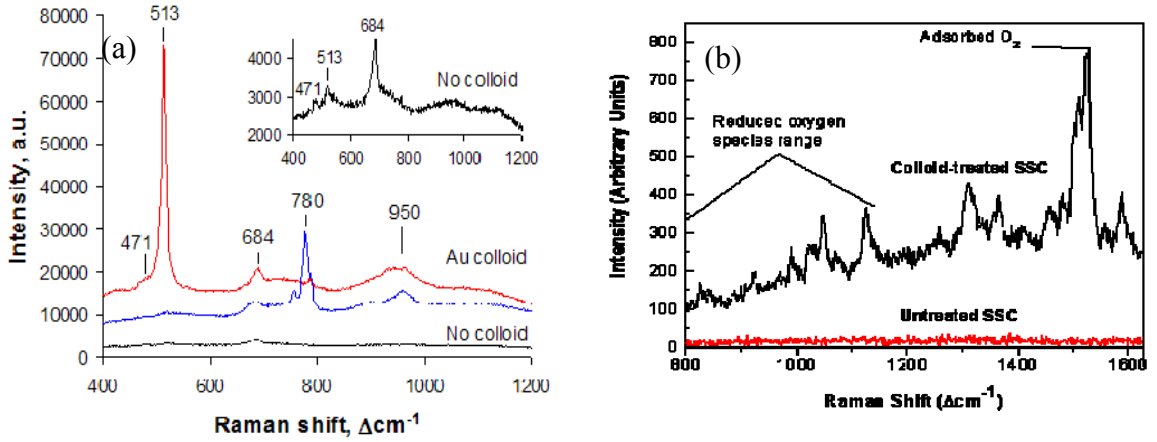

Figure 11. (a) Raman spectrum collected in air from a dense SSC pellet before (bottom spectrum) and after (top two spectra) application of a 20 nm gold colloid. The inset from the untreated sample shows that the enhanced peaks were all present before the colloid was applied. (b) Raman spectra from $Sr_{0.5}Sm_{0.5}CoO_3$ in air before and after application of Ag colloid with heat treatment at 325°C.